Accommodation of tin in tetragonal ZrO$_2$

B. D. C. Bell,[1] S. T. Murphy,[2] P. A. Burr,[1,3] R. W. Grimes,[1] and M. R. Wenman[1,a)]

[1]*Department of Materials and Centre for Nuclear Engineering, Imperial College, London SW7 2AZ, United Kingdom*
[2]*Department of Physics and Astronomy, University College London, Gower Street, London WC1E 6BT, United Kingdom*
[3]*Institute of Materials Engineering, Australian Nuclear Science & Technology Organisation, Menai, New South Wales 2234, Australia*

Atomic scale computer simulations using density functional theory were used to investigate the behaviour of tin in the tetragonal phase oxide layer on Zr-based alloys. The $Sn_{Zr}^{\times}$ defect was shown to be dominant across most oxygen partial pressures, with Sn_{Zr}'' charge compensated by $V_O^{\bullet\bullet}$ occurring at partial pressures below 10^{-31} atm. Insertion of additional positive charge into the system was shown to significantly increase the critical partial pressure at which Sn_{Zr}'' is stable. Recently developed low-Sn nuclear fuel cladding alloys have demonstrated an improved corrosion resistance and a delayed transition compared to Sn-containing alloys, such as Zircaloy-4. The interaction between the positive charge and the tin defect is discussed in the context of alloying additions, such as niobium and their influence on corrosion of cladding alloys. © 2015 AIP Publishing LLC.
[http://dx.doi.org/10.1063/1.4909505]

I. INTRODUCTION

A. Corrosion of zirconium

Zirconium alloys are used in pressurised water reactors due to their low capture cross-section for thermal neutrons, high corrosion resistance, and acceptable mechanical properties. Initially, corrosion follows an approximately cubic rate law.[1] After a few microns of oxide growth, there is a sudden increase in the corrosion rate as the protective layer breaks down; this process is generally referred to as transition or break-away corrosion. Post-transition, a reduced corrosion rate is again observed. This process repeats in a cycle; the time from initial corrosion to transition and subsequent later transitions is also composition dependent.[1,2]

During corrosion, hydrogen is produced, which arrives at the metal oxide interface. Hydrogen has a low solubility in ZrO$_2$ so that after recombining with electrons, the hydrogen atoms move either into the coolant, or into the oxygen-saturated α-Zr beneath the oxide (in which hydrogen exhibits a much higher solid solubility[3]). When the solubility limit for hydrogen in α-Zr is exceeded, zirconium hydrides precipitate. The fraction of hydrogen produced during corrosion, which moves into the cladding metal, is called the hydrogen pick-up fraction (HPUF) and is alloy dependent. It has been suggested[4] that alloys which exhibit a lower HPUF have a more electrically conductive oxide layer, allowing ion-electron recombination to occur further from the metal-oxide interface thereby lowering the probability of the hydrogen entering the cladding metal. A lower HPUF is desirable, since there is a regulatory upper limit to the amount of hydrogen allowed in the cladding metal.[5]

B. Oxide layer composition

Various experimental techniques have demonstrated that the pre-transition oxide layer formed on the surface of zirconium alloys is composed of several distinct regions. From the outside inwards: an outer layer of predominantly columnar monoclinic ZrO$_2$, a 50–80 nm layer containing equiaxed tetragonal ZrO$_2$, often a 100–200 nm layer of sub-stoichiometric Zr-oxide, and finally α-Zr metal (saturated with oxygen close to the metal-oxide interface) can be seen.[6–8]

Early studies of the sub-stoichiometric oxide layer were unable to identify the crystal structure other than it resembled distorted α-Zr.[9] Subsequent TEM work hinted at several possible sub-stoichiometric zirconia structures, such as cubic ZrO (Refs. 10 and 11) or an ordered oxygen solid solution within ω-Zr with an approximate stoichiometry of Zr$_3$O.[12] Random structure searching of the Zr-system using density functional theory (DFT) has identified previously unknown energetically stable structures,[13,14] recent studies have identified a metastable ZrO structure, with an HCP lattice similar to α-Zr.[15,16]

It is generally agreed that an increased proportion of tetragonal ZrO$_2$ phase is found adjacent to the metal-oxide interface, where it is stabilised by a combination of grain size, compressive stress, and the presence of alloying (i.e., dopant) elements.[17–19] Immediately post-transition, oxides have been shown to contain very little tetragonal or sub-stoichiometric zirconia away from the metal oxide interface, suggesting that these phases are transformed to monoclinic ZrO$_2$ during transition.[9]

At the metal oxide interface, the oxygen partial pressure is expected to be extremely low, however the limited amount of atom probe[20] and TEM (Ref. 21) studies thus far have demonstrated that a significant variation from ZrO$_2$ stoichiometry is not observed; instead a sharp transition occurs from ZrO$_2$ to ZrO over a distance of a few nm, with a more

a)Author to whom correspondence should be addressed. Electronic mail: m.wenman@imperial.ac.uk

gradual change from ZrO to oxygen-saturated α-Zr occurring over a distance of tens of nm.

C. Oxide phase stability

Various investigations have demonstrated the presence of high compressive stresses (0.2–3 GPa) in the oxide layer in the plane of the oxide-metal interface,[22–25] due to the Pilling-Bedworth ratio of 1.56 on converting from zirconium to ZrO$_2$. Experimental work had shown that applied hydrostatic stress can stabilise the metastable tetragonal ZrO$_2$ phase due to it having a smaller volume than the monoclinic phase.[26,27] Recent synchrotron x-ray diffraction (XRD) work performed by Ortner *et al.*[28] has demonstrated a significant variation in the stress through the oxide layer, with higher in-plane compressive stresses observed close to the metal-oxide interface. Similar work performed by Polatidis *et al.* also identified a discontinuity in the stress profile, with a sudden increase in compressive stress at a depth within the oxide layer, which had previously been identified, using electron microscopy, as the approximate point of transition from monoclinic to tetragonal rich ZrO$_2$.[23]

Small grain sizes (typically less than 30 nm) can also result in tetragonal phase stability with no additional environmental factors.[17,29,30] Qin *et al.*[31] combined these theories into a thermodynamic model, suggesting that in any given environment, there is a critical grain size below which the tetragonal phase is stable. Applied stress increases this critical grain size allowing more tetragonal phase to be stabilised.

Dopant stabilisation can occur due to the incorporation of larger cations that expand the oxide lattice, or by the incorporation of lower valence cations, which stabilise the tetragonal and cubic fluorite phases by the incorporation of oxygen vacancies. While the concentrations of dopant elements required for complete cubic phase stabilisation (e.g., 20 mol% yttrium[32]) are far higher than the concentration of alloying elements in any common zirconium based alloys, concentrations as low as 2 mol% yttrium can stabilise the tetragonal phase.[33] When the other complementary stabilisation methods (stress and grain size) are present, it is possible that even 1–2% of trivalent and divalent cations could have a stabilising effect.

D. Tin as an alloying addition

Tin was added initially to reduce the detrimental effects of nitrogen and carbon impurities, and is still present in Zircaloy-2 and Zircaloy-4 as it also improves strength and creep resistance.[34] It has, however, been demonstrated that the removal of tin from modern cladding alloys can increase the time until transition occurs and lower HPUF.[35–38]

Unlike many other alloying elements, the amount of tin included is lower than the solid solubility limit in α-Zr, so that a homogeneous distribution throughout the cladding matrix is expected. Wei *et al.*[35] observed that in the oxide layers of various Zr-Sn-Nb alloys, those with lower tin content exhibited a smaller proportion of pre-transition tetragonal phase. A reduction in the corrosion rate, due to a delayed transition, was also observed, implying a correspondence

with tetragonal phase fraction, tin content, and corrosion rate, which had not previously been suggested.

In this study, the behaviour of tin as a substitutional and interstitial defect in tetragonal ZrO$_2$ is investigated using computer simulation. Quantum mechanical calculations using density functional theory are performed and comparisons are made to previous experimental data concerning the corrosion of tin-containing zirconium alloys.

II. METHODOLOGY

Simulations were performed using the density functional theory based CASTEP 6.11 code.[39] Ultra-soft pseudo potentials with a cut-off energy of 550 eV were used throughout. The Perdew, Burke, and Ernzerhof[40] parameterisation of the generalised gradient approximation was employed to describe the exchange correlation function. A Monkhorst-Pack sampling scheme[41] was used for the integration of the Brillouin Zone with a minimum k-point separation of 0.045 Å^{-1}. The simulations employed density mixing using the Pulay method.[42]

The energy convergence criterion for self-consistent calculations was set to 1×10^{-8} eV and the maximum allowed forces between ions was 1×10^{-2} eV/Å. All simulations were performed until a maximum difference in energy of 1×10^{-5} eV and atomic displacement of 5×10^{-4} Å between iterations was achieved.

Non-defective structures were relaxed under constant pressure to the above convergence criteria. All defective structures were generated from pre-relaxed non-defective structures, and were energy minimised under constant volume (cell parameters constrained to maintain the shape and volume of the perfect supercell) in order to approximate dilute conditions. A supercell was formed from $3 \times 3 \times 2$ repetitions of the tetragonal ZrO$_2$ unit cell in the x, y, and z directions, respectively. This resulted in a 108 atom supercell, which offered a reasonable compromise between reducing finite size effects and computation time.

A. Defect formation energies

The defect formation energies (E^{f}) of intrinsic defects were calculated using the following equation, where a point defect X with charge q is formed in a perfect cell:

$$E^{\mathrm{f}}_{X^q} = E^{\mathrm{DFT}}_{X^q_{Zr}} - E^{\mathrm{DFT}}_{\mathrm{perfect}} \pm \sum_i n_i \mu_i + q(E_{\mathrm{VBM}} + \mu_e) + E_{\mathrm{MP}},$$

(1)

$E^{\mathrm{DFT}}_{\mathrm{perfect}}$ is the energy of the perfect cell, $E^{\mathrm{DFT}}_{X^q_{Zr}}$ is the energy of the defective cell, E_{VBM} is the valence-band maximum (VBM) of the perfect supercell, n_i is the number of atoms added/removed, and μ_i is the chemical potential of the defect species added/removed. E_{MP} is an energy correction calculated using the Makov-Payne method[43] to account for the electrostatic self-interaction of defects caused by the use of periodic boundary conditions and a finite supercell size. μ_e is the chemical potential of electrons relative to E_{VBM}; taking values of μ_e at the VBM and conduction-band minimum, the

defect formation energy can be plotted as a function of μ_e across the band gap of the material.[44,45]

B. Chemical potentials

For a given set of conditions, the sum of the chemical potentials (μ) per formula unit of the constituent species equals the total Gibbs free energy of the solid ZrO_2, leading to the following relationship:

$$\mu_{ZrO_2(s)} = \mu_{Zr}(T, p_{O_2}) + \mu_{O_2}(T, p_{O_2}), \quad (2)$$

where T is the temperature and p_{O_2} is the oxygen partial pressure. In order to avoid the well-known difficulties regarding the inability of DFT to accurately describe the O_2 molecule, we adopt an approach first used by Finnis *et al.*[46] This avoids the necessity to calculate the oxygen chemical potential in DFT by instead using the known experimental formation energy of the ZrO_2 oxide, and calculating the chemical potential of oxygen at standard temperature and pressure using the following relationship:

$$\Delta G_f^{ZrO_2} = \mu_{ZrO_2(s)} - \mu_{Zr(s)} - \mu_{O_2}(T^\circ, p_{O_2}^\circ). \quad (3)$$

We assume the Gibbs free energy is independent of temperature for the solid species, however for the gaseous O_2, this assumption does not hold true. Instead the oxygen chemical potential at the temperature of interest $\mu_{O_2}(T, p_{O_2})$ is extrapolated from the standard state $\mu_{O_2}(T^\circ, p_{O_2}^\circ)$ using the ideal gas relationship. The full expression for the oxygen chemical potential is as follows:

$$\mu_{O_2}(T, p_{O_2}) = \mu_{O_2}(T^\circ, p_{O_2}^\circ) + \Delta\mu(T) + \frac{1}{2}k_B \log\left(\frac{p_{O_2}}{p_{O_2}^\circ}\right), \quad (4)$$

and the rigid-dumbell ideal gas for $\Delta\mu(T)$ can be given by

$$\Delta\mu(T) = -\frac{1}{2}\left(S_{O_2}^\circ - C_P^\circ\right)(T - T^\circ) + C_P^\circ T \log\left(\frac{T}{T^\circ}\right), \quad (5)$$

where $S_{O_2}^\circ$ is the molecular entropy at standard temperature and pressure and C_P° is the constant pressure heat capacity of oxygen gas. Values for these two properties were obtained from the literature with $S_{O_2}^\circ = 0.0021\,eV/K$ and $C_P^\circ = 7k_B = 0.000302\,eV/K$.[47]

Tetragonal ZrO_2 is not stable under standard conditions, so the free energy of formation was calculated by adding the energy difference between monoclinic and tetragonal ZrO_2 (as calculated at 0 K by DFT) to the experimentally determined value for the free energy of formation of monoclinic ZrO_2, this resulted in a value of $-11.41\,eV$.

C. Brouwer diagram

The sum of all defects each multiplied by their charge must equal zero, since there is no overall charge on the crystal. This can be expressed as follows:

$$\sum_i q_i c_i - N_c \exp\left(-\frac{E_g - \mu_e}{k_B T}\right) + N_v \exp\left(-\frac{\mu_e}{k_B T}\right) = 0, \quad (6)$$

where the first term is the sum of the charges of all ionic defects, the second term is the electron concentration, and the third term the hole concentration in the crystal. N_c and N_v are the density of states for the conduction and valence bands and E_g is the band gap of the crystal. Tetragonal ZrO_2 is an insulating material and so the concentrations of electrons and holes are expected to be sufficiently low that Boltzmann statistics are appropriate. The formation energy for an electron in the conduction band will be slightly lower than the value calculated by $E_g - \mu_e$ due to self trapping of electrons. However, in a wide band gap insulator, such as ZrO_2, the difference in energy will be minimal and so this is an acceptable approximation.

Using this relationship, the electron chemical potential that ensures charge neutrality in the system can be calculated for any given elemental chemical potential. Using this, the concentration of individual defects can be calculated and by plotting these as a function of oxygen partial pressure, a Brouwer diagram is constructed.

III. RESULTS AND DISCUSSION

A. Interstitials

Potential interstitial sites were chosen by considering the Wyckoff positions of the space group for tetragonal ZrO_2 ($P4_2/nmc$). The 2b and 4c positions are very similar, however both were included to investigate whether there was a preference to be closer to a zirconium cation (as in the case of the 4c position) or a position equidistant between two (as in the 2b position). An interstitial ion was placed in each non-identical site and an overall charge was applied to the supercell corresponding to the charge state of the interstitial ion; -2 to 0 for oxygen, 0 to $+4$ for zirconium and tin. A list of the non-identical sites considered, along with the corresponding lattice co-ordinates is reported in Table I.

A successful convergence was only achieved for oxygen in the 2b location, suggesting that the other sites are not stable for any charge state. Convergence was achieved for zirconium and tin interstitials on all sites; for both, the 2b site was preferred. Tin and zirconium interstitials placed at the 4c site migrated to the 2b site during the simulation and the 4d site was not energetically favourable for any interstitials, generally exhibiting a formation energy of several eV higher than the 2b site.

B. Defect formation energies

The defect formation energies for single isolated defects as a function of μ_e calculated using Eq. (1) are shown in

TABLE I. A list of the non-identical Wyckoff positions for tetragonal ZrO_2 considered as possible interstitial sites.

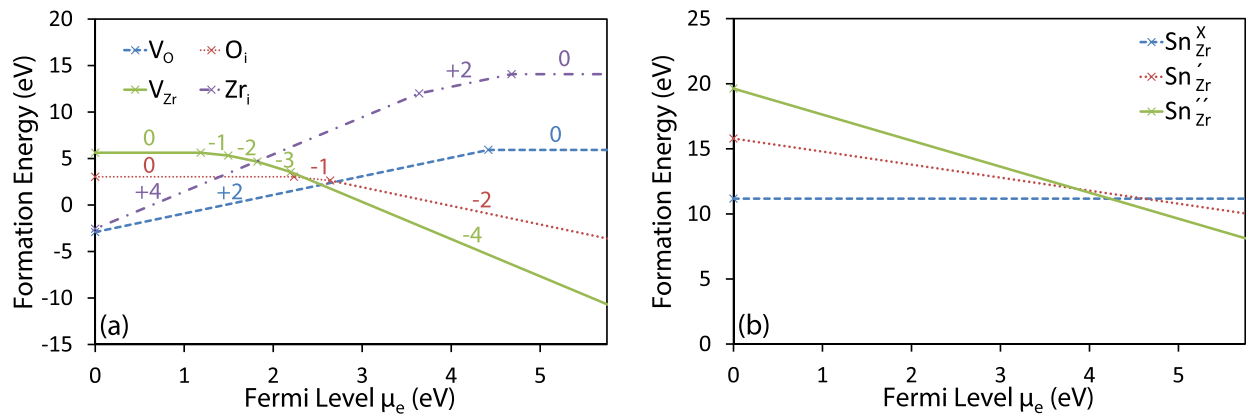| Position	*a*	*b*	*c*
2b	0	0	0.5
4c	0	0	−0.25
4d	0.5	0	0

FIG. 1. Formation energies of intrinsic defects (a) and tin substitutional defects (b) as calculated by Eq. (1) using DFT calculated energies from a reference state of $Zr_{(s)}$ and plotted as a function of the Fermi level (μ_e), from the VBM across the experimental band gap of 5.75 eV.[51]

Figure 1. Oxygen defects exist almost entirely in the fully charged or zero charged states, implying that the singly charged state is not thermodynamically favourable for either a vacancy or interstitial.

Zirconium vacancies exist in the -4 oxidation state across the majority of the band gap, with a transition through all charge states to 0 observed close to the VBM. The zirconium interstitial is also observed in the fully charged $+4$ state across the majority of the band gap, transitioning to $+2$ and then 0 close to the conduction band minimum (CBM). These observations agree well with previous simulation work investigating tetragonal ZrO_2.[48–50]

Tin interstitial defects are predicted to have a very high formation energy when compared to other possible defects and so can be assumed to exhibit a negligible concentration. The formation energies for the substitutional Sn_{Zr} defect are shown in Figure 1. The $Sn_{Zr}^{\times}$ defect is favoured across the majority of the band gap, with a transition to Sn_{Zr}'' occurring close to the CBM. The Sn_{Zr}' defect is not observed at any point in the band gap, this is expected as it would otherwise require tin to be in the $+3$ charge state which would result in an energetically unfavourable unpaired s-orbital electron.

C. Brouwer diagram

Following the methodology discussed in Sec. II C, Brouwer diagrams were constructed for intrinsic tetragonal ZrO_2 and for tin doped ZrO_2, and are shown in Figure 2. As discussed in Sec. I C, tetragonal ZrO_2 is stabilised in the undoped oxide layer by a combination of grain size and compressive stress. In this work, stress was not applied and so the Brouwer diagrams were plotted at 1500 K, the approximate temperature at which tetragonal phase is stable under standard conditions, rather than at a normal reactor operation temperature of around 600 K. In this regard, we follow the approach used in previous DFT studies on the tetragonal system.[48,52]

In the intrinsic case (Figure 2(a)) at very low oxygen partial pressures, the uncharged oxygen vacancy appears. However, across the majority of the oxygen partial pressures considered, the dominant structural defect is the fully charged oxygen vacancy, charge compensated by electrons. Only at the highest oxygen partial pressures, the fully charged zirconium vacancy, charge compensated by holes, begin to appear.

The diagram that includes substitutional tin (Figure 2(b)) indicates that $Sn_{Zr}^{\times}$ is dominant across the majority of
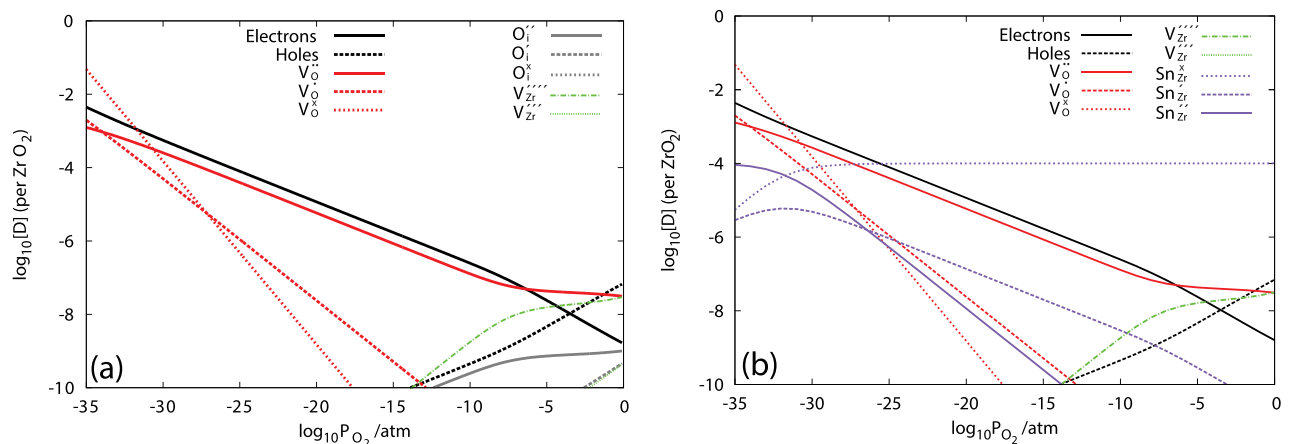

FIG. 2. Brouwer diagram showing the concentrations of point defects in tetragonal ZrO_2 as a function of oxygen partial pressure at 1500 K. (a) is the intrinsic system and (b) contains tin at a concentration of 1×10^{-4} at. %.
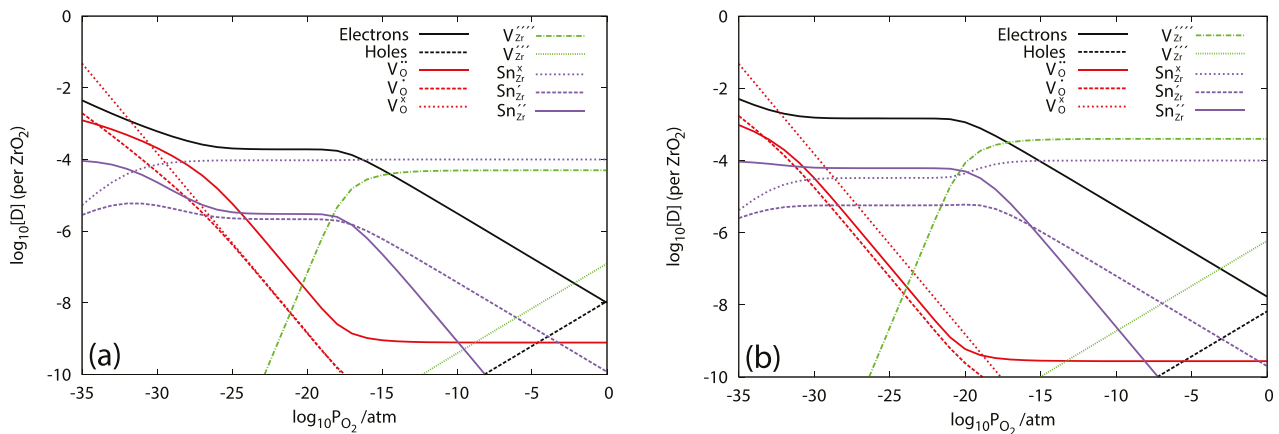
FIG. 3. Brouwer diagrams containing tin at a concentration of 1×10^{-4} at. % and an additional defect of charge $+1$ ($q = 1$) inserted into the calculation via Eq. (6); (a) $c = 5 \times 10^{-4}$ and (b) $c = 2 \times 10^{-3}$.

oxygen partial pressures considered, with a transition to Sn''_{Zr} charge compensated by $V^{\bullet\bullet}_O$ occurring at partial pressures below 10^{-31} atm.

D. Tin interaction with other alloying elements

Tin has been shown to have little effect on the corrosion resistance and no measurable effect on HPUF in Zr-Sn binary alloys.[53] As previously discussed, the tin Brouwer diagrams (Figure 2) suggest that tin exists as $Sn^{\times}_{Zr}$ until extremely low oxygen partial pressures. Given that Sn^{4+} and Zr^{4+} occupy the same lattice site, have similar ionic radii and exist in the same oxidation state, it is perhaps unsurprising that the $Sn^{\times}_{Zr}$ defect has little measurable effect on the chemistry of the system. However, Sn-Zr binary alloys are not used in any reactor applications and so we must consider the effect of further alloying additions.

Niobium containing alloys have been developed with excellent corrosion and HPUF resistance, and recent experimental work has suggested that the removal of tin, included for its positive effect on the mechanical properties of the alloys, improves the corrosion resistance still further.[35] Given that tin in isolation has no effect on the corrosion and HPUF properties, it seems plausible that there is an interaction between tin and niobium in the alloys.

Niobium is generally assumed to exist in the Nb^{5+} state within the oxide layer. If we assume the 5+ state, this results in a predominant $Nb^{\bullet}_{Zr}$ defect, which agrees with DFT simulations by Otgonbaatar.[54] This would lead to the injection of positive charge into the oxide layer. Nevertheless, this assumption has been challenged recently through x-ray absorption near-edge structure (XANES) work which instead suggests the charge state is between 2+ and 4+.[55,56] Recent theoretical and experimental works by Couet *et al.*[57] have suggested another possible source of positive charge close to the metal-oxide interface due to a space charge effect caused by the non-equilibrium distribution of electrons in the insulating oxide layer.

In order to consider the effect of the positive charge, an additional defect was added to the first term of Eq. (6). This defect was given a charge of $+1$, and a Brouwer diagram

was plotted for a range of concentrations. The inclusion of an additional positive defect at a concentration of 5×10^{-4} (Figure 3(a)) causes the concentration of V''''_{Zr} to dramatically increase and also lowers the concentration of $V^{\bullet\bullet}_O$ and $V^{\bullet}_O$ (the concentration of $V^{\times}_O$ is unchanged since it is not charged and therefore unaffected by charge difference in the system). Importantly, although the concentration of Sn''_{Zr} is increased, $Sn^{\times}_{Zr}$ remains the dominant defect at partial pressures above 10^{-31} atm.

Increasing the concentration of applied charge further (Figure 3(b)) causes Sn''_{Zr} to become the dominant tin defect up to a partial pressure of 10^{-20} atm. This increase in around 10 orders of magnitude happens at a critical charge concentration and as demonstrated by Figure 4 even large changes in charge above or below this critical value have little effect on the crossover point. The critical charge at which transition occurs appears to be strongly dependent on temperature, with an increase in 500 K causing the value to increase by an order of magnitude, suggesting that the $Sn^{\times}_{Zr}$ defect is more favourable at higher temperatures. The existence of a critical value has previously been predicted in sapphire by Lagerlöf and Grimes,[58] who observed that a critical doping level caused the concentration of oxygen vacancies to change by
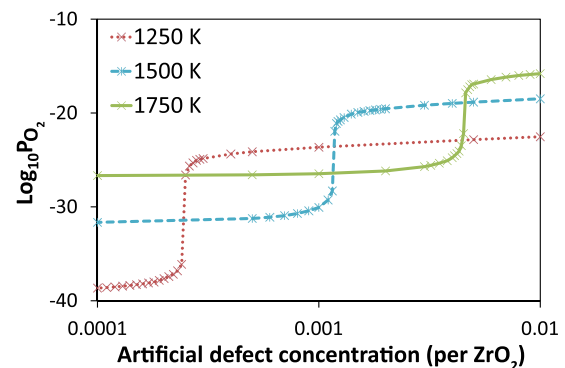

FIG. 4. A chart showing the oxygen partial pressure at which the $Sn^{\times}_{Zr}/Sn''_{Zr}$ transition occurs as a function of the applied additional charge; 1250 K at a concentration of $(2.4–2.5) \times 10^{-4}$, 1500 K at $(1.15–1.18) \times 10^{-3}$, 1750 K at $(4.5–4.6) \times 10^{-3}$.

10–20 orders of magnitude. Interestingly, as the temperature of the Brouwer diagram calculation was increased, the change in partial pressure observed at the critical doping level reduced.

E. Implications for corrosion resistance and HPUF

It is generally assumed that niobium improves corrosion resistance by suppressing the formation of oxygen vacancies in the bulk oxide, thereby reducing the oxygen ion conductivity. This is achieved due to the positive charge introduced by the dominant $Nb^{\bullet}_{Zr}$ defect, which suppresses $V^{\bullet\bullet}_O$ and $V^{\bullet}_O$ since they are also positively charged. However, as demonstrated in Figures 3 and 4, the presence of a concentration of positive charge in the system causes the $Sn^{\times}_{Zr}$ defect to become Sn''_{Zr}. Considering the oxide layer on a Zr-Sn-Nb type alloy, this tin behaviour would negate the oxygen vacancy suppression delivered by niobium by charge compensating $Nb^{\bullet}_{Zr}$ defects, suggesting a possible mechanism by which tin diminishes the corrosion resistance of Zr-Sn-Nb alloys.

As mentioned in the introduction, oxygen vacancies can have the effect of stabilising the tetragonal phase. Thus, a further interesting implication is that the increased $V^{\bullet\bullet}_O$ concentration in Sn-containing Nb-Zr alloys could result in the increased tetragonal phase fraction observed in XRD work by Wei *et al.*[35] As corrosion progresses, the metal-oxide interface will move further away from the Sn''_{Zr} substitutional defects interface due to the thickening of the oxide layer, which will have the effect of increasing the oxygen partial pressure in the oxide surrounding the defects. As demonstrated by Figures 3 and 4, there is a critical partial pressure at which the Sn''_{Zr} defect will reduce to $Sn^{\times}_{Zr}$. As this reduction occurs, the increased $V^{\bullet\bullet}_O$ concentration associated with the presence of Sn''_{Zr} is no longer expected. Thus, the stabilisation mechanism causing the increased tetragonal phase volume will no longer exist and a transformation to monoclinic phase will occur. The tetragonal to monoclinic phase transformation is associated with a volume increase of approximately 4%[59] and so cracking of the oxide layer is expected. This process could lead to an earlier onset of transition than would otherwise occur, a conclusion that agrees closely with experimental observations that the reduction of Sn content delays the first transition significantly.[35]

IV. CONCLUSIONS

DFT simulations were used to investigate the defect properties of intrinsic and Sn-doped tetragonal ZrO_2. The intrinsic case agreed well with previous DFT work performed by Youssef *et al.*[48] Tin is predicted to exhibit a 4+ charge state and exist almost entirely in uncharged $Sn^{\times}_{Zr}$, transitions to a 2+ charge state and thus Sn''_{Zr} only at oxygen partial pressures below 10^{-31} atm.

An additional positively charged defect was included in the Brouwer diagram calculations to account for the effect of positively charged defect species, in particular, $Nb^{\bullet}_{Zr}$. It is predicted that up to a critical concentration, the additional defect has little effect on the dominance of $Sn^{\times}_{Zr}$ defect, with the only observed effect being the suppression of oxygen

vacancies and increased concentration of zirconium vacancies, as would be expected in a Nb-containing system. Above a temperature dependent critical concentration, however, the additional positive charged defect promotes the transition from $Sn^{\times}_{Zr}$ to Sn''_{Zr} to occur at an oxygen partial pressure of many orders magnitude higher. The concentration at which this change occurs and the magnitude of the change in partial pressure has a strong temperature dependence, a higher charge concentration was required at high temperatures but resulting in a smaller shift in partial pressure.

It is suggested that this change in tin oxidation state will inhibit the oxygen vacancy suppression, which would otherwise be caused by the additional positive charge, thereby accounting for the increased corrosion rate and shorter time to transition observed in Zr-Sn-Nb type alloys when compared to similar alloys containing niobium but no tin. With no niobium content, we expect tin to maintain an overall neutral charge ($Sn^{\times}_{Zr}$) and therefore have little effect on the corrosion performance or time to transition. This provides a model framework by which we can interpret experimental work on Zn-Sn binary alloys.[53]

[1]E. Hillner, "Corrosion of Zirconium-Base Alloys—An Overview," *Zirconium in the Nuclear Industry Proceedings of the Third International Conference, ASTM STP 633*, edited by A. L. Lowe, Jr. and G. W. Parry (American Society for Testing and Materials, 1977), pp. 211–235.

[2]J. S. Bryner, "The cyclic nature of corrosion of Zircaloy-4 in 633 K water," J. Nucl. Mater. **82**, 84–101 (1979).

[3]M. Miyake, M. Uno, and S. Yamanaka, "On the zirconium-oxygen-hydrogen ternary system," J. Nucl. Mater. **270**, 233–241 (1999).

[4]A. Couet, "Hydrogen pick-up behaviour in zirconium alloys," Ph.D. thesis (Pennsylvania State University, 2011).

[5]P. Raynaud and A. Bielen, "Cladding hydrogen based regulations in the United States," *2011 Water Reactor Fuel Performance Meeting Chengdu, China, 11–14 Sept. 2011*, T3–031.

[6]H. J. Beie, "Examinations of the corrosion mechanism of zirconium alloys," *Zirconium in the Nuclear Industry: Tenth International Symposium, ASTM STP 1245*, edited by A. M. Garde and E. R. Bradley (American Society for Testing and Materials, Philadelphia, 1994), pp. 615–643.

[7]M. Preuss, P. Frankel, S. Lozano-Perez, D. Hudson, E. Polatidis, N. Ni, J. Wei, C. English, S. Storer, K. B. Chong, M. Fitzpatrick, P. Wang, J. Smith, C. R. M. Grovenor, G. Smith, J. Sykes, B. Cottis, S. Lyon, L. Hallstadius, B. Comstock, A. Ambard, M. Blat-Yrieix, P. Barberis, and S. W. Dean, "Studies regarding corrosion mechanisms in zirconium alloys," J. ASTM Int. **8**(9), 649–681 (2011).

[8]A. Garner, M. Preuss, and P. Frankel, "A method for accurate texture determination of thin oxide films by glancing-angle laboratory X-ray diffraction," J. Appl. Crystallogr. **47**(2), 575–583 (2014).

[9]H. Anada and K. Takeda, "Microstructure of oxides on Zircaloy-4, 1.0 Nb Zircaloy-4, and Zircaloy-2 formed in 10.3-MPa steam at 673 K," *Zirconium in the Nuclear Industry: Eleventh International Symposium, ASTM STP 1295*, edited by E. R. Bradley and G. P. Sahol (American Society for Testing and Materials, 1996), pp. 35–54.

[10]P. T. Moseley and B. Hudson, "Phases involved in the corrosion of zircaloy by hot water (350 °C)," J. Nucl. Mater. **99**, 340–344 (1981).

[11]T. Furuta and H. Motohashi, "Products at the surface of zircaloy cladding under loca conditions," J. Nucl. Mater. **95**, 303–306 (1980).

[12]X. Iltis and H. Michel, "Transmission electron microscopy study of a locally ordered Zr–O solid solution obtained by an oxidation treatment of a Zircaloy-4 alloy," J. Alloys Compd. **177**, 71–82 (1991).

[13]S. C. Lumley, S. T. Murphy, P. A. Burr, R. W. Grimes, P. R. Chard-Tuckey, and M. R. Wenman, "The stability of alloying additions in Zirconium," J. Nucl. Mater. **437**(1–3), 122–129 (2013).

[14]H. Wang, A. Chroneos, C. Jiang, and U. Schwingenschlögl, "Modelling zirconium hydrides using the special quasirandom structure approach," Phys. Chem. Chem. Phys. **15**(20), 7599–7603 (2013).

[15]B. Puchala and A. Van der Ven, "Thermodynamics of the Zr-O system from first-principles calculations," Phys. Rev. B **88**(9), 094108 (2013).

[16]R. J. Nicholls, N. Ni, S. Lozano-Perez, A. London, D. W. McComb, P. D. Nellist, C. R. M. Grovenor, C. J. Pickard, and J. R. Yates, "Crystal structure of the ZrO phase at zirconium/zirconium oxide interfaces," Adv. Eng. Mater. **17**, 211–215 (2015).

[17]Y. Ding and D. O. Northwood, "TEM study of the oxide-metal interface formed during corrosion of Zr-2.5 wt.% Nb pressure tubing," Mater. Charact. **30**, 13–22 (1993).

[18]N. Petigny, P. Barberis, C. Lemaignan, Ch. Valot, and M. Lallement, "In situ XRD analysis of the oxide layers formed by oxidation at 743 K on Zircaloy 4 and Zr-1NbO," J. Nucl. Mater. **280**(3), 318–330 (2000).

[19]A. Yilmazbayhan, A. T. Motta, R. J. Comstock, G. P. Sabol, B. Lai, and Z. Cai, "Structure of zirconium alloy oxides formed in pure water studied with synchrotron radiation and optical microscopy: Relation to corrosion rate," J. Nucl. Mater. **324**(1), 6–22 (2004).

[20]D. Hudson, N. Ni, S. Lozano-Perez, and D. Saxey, "The atomic scale structure and chemistry of the Zircaloy-4 metal-oxide interface," in *Proceedings of the 14th International Conference on Environmental Degradation of Materials in Nuclear Power Systems, Virginia Beach, VA, 23–27 August (2009)*.

[21]N. Ni, D. Hudson, J. Wei, P. Wang, S. Lozano-Perez, G. D. W. Smith, J. M. Sykes, S. S. Yardley, K. L. Moore, S. Lyon, R. Cottis, M. Preuss, and C. R. M. Grovenor, "How the crystallography and nanoscale chemistry of the metal/oxide interface develops during the aqueous oxidation of zirconium cladding alloys," Acta Mater. **60**(20), 7132–7149 (2012).

[22]C. Roy and G. David, "X-ray diffraction analyses of zirconia films on zirconium and zircaloy-2," J. Nucl. Mater. **37**, 71–81 (1970).

[23]E. Polatidis, P. Frankel, J. Wei, M. Klaus, R. J. Comstock, A. Ambard, S. Lyon, R. A. Cottis, and M. Preuss, "Residual stresses and tetragonal phase fraction characterisation of corrosion tested Zircaloy-4 using energy dispersive synchrotron X-ray diffraction," J. Nucl. Mater. **432**(1–3), 102–112 (2013).

[24]F. Antoni, M. Pons, M. Ignat, and D. Hertz, "Approche mecano-chimique de l'oxydation du zircaloy-4," Surf. Coat. Technol. **46**, 347–360 (1991).

[25]F. Garzarolli and H. Seidel, "Oxide growth mechanism on zirconium alloys," *Zirconium in the Nuclear Industry: Ninth International Symposium, ASTM STP 1132*, edited by C. M. Eucken and A. M. Garde (American Society for Testing and Materials, Philadelphia, 1991), pp. 395–415.

[26]P. Bouvier, J. Godlewski, and G. Lucazeau, "A Raman study of the nano-crystallite size effect on the pressure-temperature phase diagram of zirconia grown by zirconium-based alloys oxidation," J. Nucl. Mater. **300**(2–3), 118–126 (2002).

[27]S. Block, J. A. H. Da Jornada, and G. J. Piermarini, "Pressure-temperature phase diagram of zirconia," J. Am. Ceram. Soc. **68**(9), 497–499 (1985).

[28]S. Ortner, H. Swan, A. Laferrere, C. English, J. Hyde, and P. Styman, "Study of zircaloy corrosion to develop mechanistic understanding," in *Contribution of Materials Investigations and Operating Experience to LWRs Safety, Performance and Reliability, France, Avignon, 14–18 September 2014*.

[29]P. Aldebert and J. P. Traverse, "Structure and ionic mobility of zirconia at high temperature," J. Am. Ceram. Soc. **68**(1), 34–40 (1985).

[30]P. Barberis, "Raman spectra of tetragonal zirconia: Powder to zircaloy oxide frequency shift," J. Nucl. Mater. **288**, 241–247 (2001).

[31]W. Qin, C. Nam, H. Li, and J. Szpunar, "Tetragonal phase stability in ZrO2 film formed on zirconium alloys and its effects on corrosion resistance," Acta Mater. **55**(5), 1695–1701 (2007).

[32]A. Bogicevic, C. Wolverton, G. Crosbie, and E. Stechel, "Defect ordering in aliovalently doped cubic zirconia from first principles," Phys. Rev. B **64**(1), 014106 (2001).

[33]X. Xia, "Computational modelling study of yttria-stabilized zirconia," Ph.D. thesis (University College London, 2010).

[34]H. S. Hong, S. J. Kim, and K. S. Lee, "Effects of alloying elements on the tensile properties and oxidation behavior of modified Zircaloy-4 in 360 °C water," J. Nucl. Mater. **238**, 211–217 (1996).

[35]J. Wei, P. Frankel, E. Polatidis, M. Blat, A. Ambard, R. J. Comstock, L. Hallstadius, D. Hudson, G. D. W. Smith, C. R. M. Grovenor, M. Klaus, R. A. Cottis, S. Lyon, and M. Preuss, "The effect of Sn on autoclave corrosion performance and corrosion mechanisms in Zr-Sn-Nb alloys," Acta Mater. **61**(11), 4200–4214 (2013).

[36]J. Schefold, D. Lincot, A. Ambard, and O. Kerrec, "The cyclic nature of corrosion of Zr and Zr-Sn in high-temperature water (633 K)," J. Electrochem. Soc. **150**(10), B451 (2003).

[37]K. Takeda and H. Anada, "Mechanism of corrosion rate degradation due to tin," in *Zirconium in the Nuclear Industry: Twelfth International Symposium, ASTM STP No. 1354*, edited by G. P. Sabol and G. D. Moan (American Society for Testing and Materials, West Conshohocken, PA, 2000), pp. 592–608.

[38]P. Barberis and A. Frichet, "Characterization of Zircaloy-4 oxide layers by impedance spectroscopy," J. Nucl. Mater. **273**, 182–191 (1999).

[39]S. J. Clark and M. D. Segall, "First principles methods using CASTEP," Z. Kristallogr. **220**, 567–570 (2005).

[40]J. Perdew, K. Burke, and M. Ernzerhof, "Generalized gradient approximation made simple," Phys. Rev. Lett. **77**(18), 3865–3868 (1996).

[41]H. J. Monkhorst and J. D. Pack, "Special points for Brillouin-zone integrations," Phys. Rev. B **13**(12), 5188–5192 (1976).

[42]P. Pulay, "Convergence acceleration of iterative sequences. The case of SCF iteration," Chem. Phys. Lett. **73**(2), 393–398 (1980).

[43]G. Makov and M. C. Payne, "Periodic boundary conditions in *ab initio* calculations," Phys. Rev. B **51**, 4014 (1995).

[44]H. A. Tahini, A. Chroneos, S. T. Murphy, U. Schwingenschloogl, and R. W. Grimes, "Vacancies and defect levels in III-V semiconductors," J. Appl. Phys. **114**(6), 063517 (2013).

[45]S. T. Murphy, M. W. D. Cooper, and R. W. Grimes, "Point defects and non-stoichiometry in thoria," Solid State Ionics **267**, 80–87 (2014).

[46]M. W. Finnis, A. Y. Lozovoi, and A. Alavi, "The oxidation of NiAl: What can we learn from *ab initio* calculations?," Annu. Rev. Mater. Res. **35**(1), 167–207 (2005).

[47]R. C. Weast, M. J. Astle, and W. H. Beyer, *CRC Handbook of Chemistry and Physics* (CRC Press Inc., Boca Raton, Florida, 1984).

[48]M. Youssef and B. Yildiz, "Intrinsic point-defect equilibria in tetragonal ZrO2: Density functional theory analysis with finite-temperature effects," Phys. Rev. B **86**(14), 144109 (2012).

[49]A. Eichler, "Tetragonal Y-doped zirconia: Structure and ion conductivity," Phys. Rev. B **64**(17), 174103 (2001).

[50]M. V. Ganduglia-Pirovano, A. Hofmann, and J. Sauer, "Oxygen vacancies in transition metal and rare earth oxides: Current state of understanding and remaining challenges," Surf. Sci. Rep. **62**(6), 219–270 (2007).

[51]R. H. French, S. J. Glass, F. S. Ohuchi, Y. N. Xu, and W. Y. Ching, "Experimental and theoretical determination of the electronic structure and optical properties of three phases of ZrO2," Phys. Rev. B **49**(8), 5133 (1994).

[52]U. Otgonbaatar and W. Ma, "Effect of niobium on the defect chemistry and oxidation kinetics of tetragonal ZrO2," J. Phys. Chem. C **118**, 20122–20131 (2014).

[53]W. E. Berry, D. A. Vaughan, and E. L. White, "Hydrogen pickup during aqueous corrosion of zirconium alloys," Corrosion **17**(3), 109t–117t (1961).

[54]U. Otgonbaatar, "The effect of niobium on the defect chemistry and corrosion kinetics of tetragonal ZrO2: A density functional theory study," Masters thesis, Massachusetts Institute of Technology, 2013.

[55]A. Froideval, C. Degueldre, C. U. Segre, M. A. Pouchon, and D. Grolimund, "Niobium speciation at the metal/oxide interface of corroded niobium-doped Zircaloys: A X-ray absorption near-edge structure study," Corros. Sci. **50**(5), 1313–1320 (2008).

[56]A. Couet, A. T. Motta, B. de Gabory, and Z. Cai, "Microbeam X-ray absorption near-edge spectroscopy study of the oxidation of Fe and Nb in zirconium alloy oxide layers," J. Nucl. Mater. **452**(1–3), 614–627 (2014).

[57]A. Couet, A. T. Motta, and A. Ambard, "The coupled current charge compensation model for zirconium alloy fuel cladding oxidation: I. Parabolic oxidation of zirconium alloys," Corros. Sci. (submitted).

[58]R. W. Grimes and K. P. D. Lagerlof, "The defect chemistry of sapphire," Acta Materialia **46**(16), 5689–5700 (1998).

[59]A. H. Heuer and M. Ruhle, "On the nucleation of the martensitic transformation in zirconia (ZrO2)," Acta Metall **33**(12), 2101–2112 (1985).